ADVANCED ENERGY MATERIALS
www.advenergymat.de

Ligand Mediated Assembly of CdS Colloids in 3D Porous Metal–Organic Framework Derived Scaffold with Multi-Sites Heterojunctions for Efficient CO_2 Photoreduction

*Tianxi Zhang, Tongtao Li, Minmin Gao, Wanheng Lu, Zongwei Chen, Wei Li Ong, Andrew See Weng Wong, Liming Yang, Sibudjing Kawi, and Ghim Wei Ho**

The inclusion of colloidal particles into 3D porous constructs to realize heterostructure ensembles enhances surface interactions and energy transfer that can transform the catalytic properties of conventional catalysts. However, assembling hydrophobic colloidal nanoparticles within hydrophilic 3D porous matrices to create tailored heterostructures and catalytic properties is particularly challenging. Here, a modified ligand grafting method is presented to spontaneously assemble CdS inorganic colloidal quantum dots within a metal-organic framework (MOF) derived porous framework for efficient photocatalytic CO_2 reduction. The grafted long chain molecular ligands effectively suppress phase separation and endow a molecular-recognition effect to form ordered assembly microstructures. The proof-of-concept assembly of CdS and Prussian blue analogues (PBA) derived Co_3O_4 facilitates a high density of heterojunctions formation, improving charge transfer and extended lifetimes of photo-induced electrons. Consequently, CdS/Co_3O_4 assembly exhibits exceptionally active and stable photocatalytic CO_2 reduction activity, with a CO production rate of 73.9 µmol g^{-1} h^{-1} and CO selectivity of 98.9%. Importantly, the ligand grafting method can be generalized to achieve spontaneous assembly of quantum dots within various metal organic framework derived porous scaffolds. This work provides a rational strategy for precise self-assembly of colloidal nanoparticles within porous microstructures, allowing tailored heterointerfaces for functional materials and applications.

1. Introduction

Semiconductor-based photocatalysis, which enables the direct conversion of solar energy into solar fuels likes hydrogen and hydrocarbons, is perceived as a promising and sustainable approach for renewable energy production and environmental remediation.[1–4] Photocatalysis efficiency is principally dictated by the light absorption, charge carrier generation and separation, redox capacity, and catalytic active sites, which are challenging to be completely fulfilled by a single component semiconductor.[5–7] Therefore, coupling another semiconductor to construct heterojunctions has been proposed to enable the utilization of the excited electrons from two distinct components that complement each other to achieve accelerated charge transfer and improved catalytic performance.[8,9]

Currently, heterojunctions and nanojunctions are commonly constructed using hydrothermal/solvothermal,[10] electrostatic self-assembly,[11,12] deposition-precipitation,[13] ion-exchange,[14] and electric field methods.[15] However, these

T. Zhang, T. Li, M. Gao, W. Lu, W. L. Ong, G. W. Ho
Department of Electrical and Computer Engineering
National University of Singapore
4 Engineering Drive 3, Singapore 117583, Singapore
E-mail: elehgw@nus.edu.sg
Z. Chen
Henan Institute of Advanced Technology
Zhengzhou University
Zhengzhou 450052, P. R. China
The ORCID identification number(s) for the author(s) of this article can be found under https://doi.org/10.1002/aenm.202400388

DOI: 10.1002/aenm.202400388

A. S. W. Wong
Facility for Analysis Characterization Testing and Simulation (FACTS)
Nanyang Technological University
Singapore 639798, Singapore
L. Yang, S. Kawi
Department of Chemical & Biomolecular Engineering
National University of Singapore
4 Engineering Drive 4, Singapore 117585, Singapore
G. W. Ho
Department of Materials Science and Engineering
National University of Singapore
Singapore 117575, Singapore

prevailing methods are constrained by factors such as disordered structural arrangement, insufficient interfacial contact, overly complicated pre-treatment, modification and synthesis procedures. In contrast, the colloidal self-assembly method offers an effective strategy to creating finely-tuned advanced materials with emergent properties due to its "bottom-up" precise control over material components and structure at multiple dimensions and scales. Therefore, utilizing the colloidal self-assembly method to prepare photocatalysts enables the formation of uniform structures, either by assembling into highly ordered superstructures[16] or integrating within ordered host matrices,[17–19] opening up a promising avenue for heterojunction design and construction.[20] The assembled photocatalysts exhibit both the characteristics of individual nanocrystalline particles and the unique collective behavior resulting from the mutually synchronized interaction of particle assemblage and alignment.[21] Additionally, the assembly of colloidal guest particles into a host matrix to form an ordered superstructure can fundamentally revolutionize the physical and chemical properties of encapsulated inorganic assemblies and host scaffolds, such as regulating light absorption capacity, inhibiting the recombination of photoinduced carriers, and accelerating chemical reactions.[22–24] Nonetheless, most hydrophobic inorganic colloidal nanoparticles can only be uniformly dispersed in nonpolar solvents, leading to inhomogeneity when placed in polar solvents like water and alcohols.[25,26] This phenomenon makes it particularly challenging to controllably assemble nanoparticles within multi-dimensional porous matrices composed of tightly packed, circuitous pores. The successful control of such assembly is crucial for creating tailored structures and harnessing synergistic effects necessary for achieving enhanced catalytic activity.

Other than self-assembly heterostructure construction, the accessibility of active sites while preserving high stability are also of prime significance for catalytic efficiency. Therefore, it is vital to select the appropriate colloidal particle guests and porous host for heterojunction formation. Colloidal cadmium sulphide (CdS), possesses adjustable redox potentials and light absorption capacity through the modulation of particle size,[27] surface area and surface functionalities, facilitating subsequent chemical and topographical modification.[28–30] However, CdS suffers from limitations such as significant recombination of electron-hole pairs and photo-corrosion issues. On the other hand, Co_3O_4 exhibits excellent CO_2 photo-reduction performance,[31,32] rendering it a good candidate to integrate with CdS to form heterojunctions for photocatalytic CO_2 reduction.[33,34] By utilizing a metal organic frameworks (MOF) derived Co_3O_4 porous scaffold can further endow Co_3O_4 with a high surface area and unique porous configuration, making it an ideal host for the encapsulation of photocatalytic active species CdS.[35,36]

Herein, we explicitly exploited a modified ligand grafting method to realize the spontaneous assembly of CdS inorganic colloidal nanoparticles within MOF derived porous frameworks to construct 3D heterostructure ensembles for efficient photocatalytic CO_2 reduction. The grafted long chain molecular ligands effectively inhibited phase separation to facilitate the formation of ordered assembly microstructures, akin to the molecular host-guest recognition-induced assembly. This method opens a promising avenue for photocatalysts heterojunction design, especially for accessing "hard-to-reach" 3D porous structures with confined or tortuous spaces and pores. As a demonstration, the co-assembly of CdS and Prussian blue analogues (PBA) derived Co_3O_4 is achieved through surface modification, followed by solvent destabilization (**Figure 1**). The resulting CdS/Co_3O_4 microstructures effectively promote the formation of a high density of heterojunctions, leading to enhanced charge transfer ability and prolonged lifetime of photo-induced electrons. As a result, the CdS/Co_3O_4 composites showed efficient photocatalytic CO_2 reduction activity with a CO production rate of 73.9 μmol g^{-1} h^{-1} and high CO selectivity of 98.9%. In addition, this modified ligand grafting method is also proven to be generalizable for the spontaneous assembly of 0D CdS within various metal organic framework derived porous scaffold. This work provides a confined assembly technique to control the self-assembly of colloidal nanoparticles within porous microstructures at a molecular level, demonstrating the possibility of controlling heterojunction construction and tailoring heterointerfaces for energy conversion applications.

2. Results and Discussion

Prior to co-assembly of CdS colloidal nanoparticles with PBA derived Co_3O_4, the behavior and properties of the individual CdS and Co_3O_4 were investigated. The TEM image in **Figure 2a** shows that the CdS nanoparticles are fairly uniform in size and are monodispersed without any agglomeration. These CdS nanoparticles have an average particle size of 3.6 nm (Figure 2b; Figure S1, Supporting Information), demonstrating the uniformity and monodispersity of CdS colloidal particles, which will be beneficial for the subsequent anchoring and immobilization of CdS within the pores of guest supports. Porous Co_3O_4 framework was obtained from the air calcination of Co-Co PBA nanocubes (chemical formula is $Co_3[Co(CN)_6]_2$). Due to the spontaneous contraction of Co-Co PBA during the calcination process, the surface of the shrunken Co_3O_4 nanoboxes became quite rough, compared to the smooth surfaces of Co-Co PBA solid cubes (Figure 2c; Figure S2, Supporting Information). Ligand decomposition during the calcination led to the formation of framework composed of small Co_3O_4 particles, forming a close-packed porous structure between particles (Figure S3, Supporting Information). This observation is supported by the Brunauer–Emmett–Teller (BET) results of the surface areas and pore size distributions of Co-Co PBA and Co_3O_4. The surface area of Co-Co PBA was determined to be 268.16 m^2 g^{-1}, while that of Co_3O_4 sample has decreased to merely 11.05 m^2 g^{-1}, resulting from the change of pore structures after calcination treatment (Figure S4, Supporting Information).[37] Consequently, the porous Co_3O_4 nanoboxes composed of numerous nanoparticles will advantageously provide ample pores or interstitial spaces between the nanograins junctions, facilitating the assemble of CdS colloidal nanoparticles.

Notably, oleic acid on the CdS surface serves as capping agent for the nucleation and growth of colloidal CdS nanoparticles, thus producing monodispersed, uniformly sized and stabilized CdS nanoparticles. However, pristine Co_3O_4 deriving from PBA exhibits obvious hydrophilicity (Figure S5, Supporting Information), which causes the occurrence of phase separation when drying a hexane dispersion containing oleate-capped CdS and PBA derived Co_3O_4 (Figure S6, Supporting Information). Therefore,

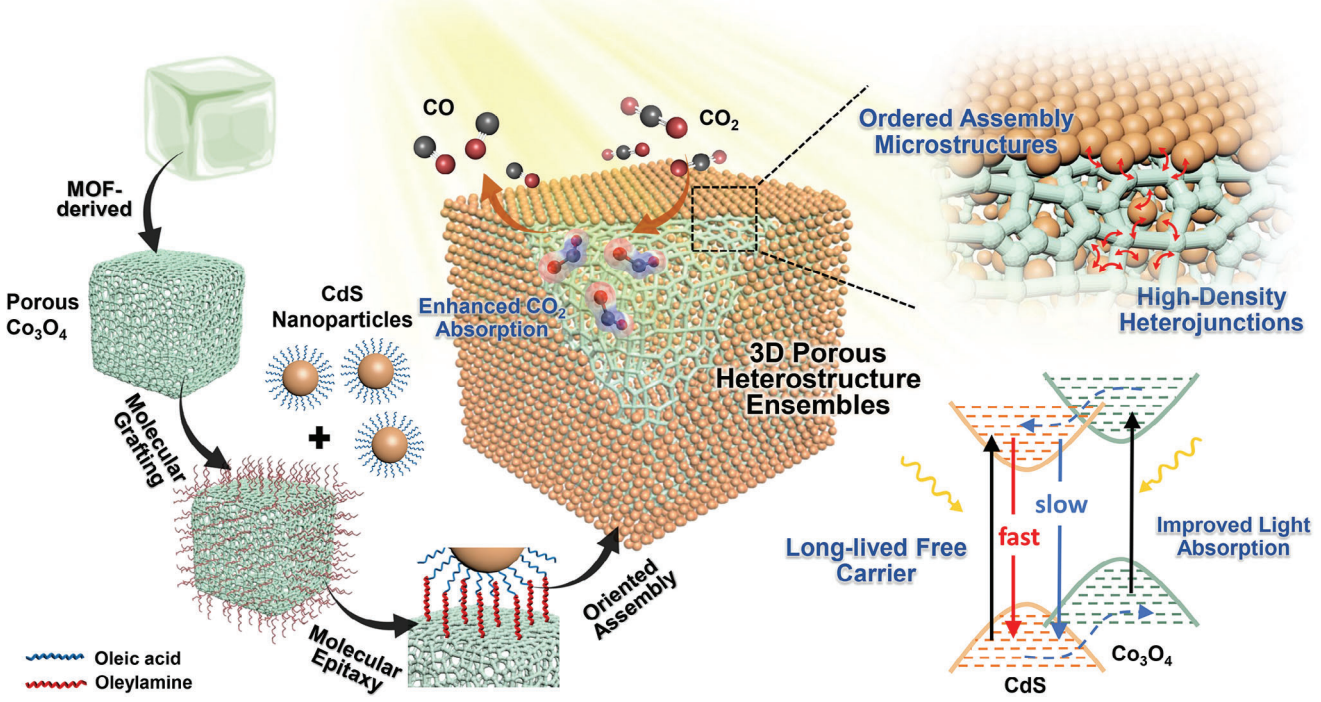

Figure 1. Schematic diagram of ligand mediated CdS/Co_3O_4 spontaneous assembly with a high density of heterojunctions and enhanced charge transfer for photocatalytic CO_2 reduction.

the surface modification to endow Co_3O_4 with the desired hydrophobicity is essential for subsequent ligand-mediated assembly. The successful functionalization of oleylamine molecules with grafted carboxylate groups on the Co_3O_4 surface is confirmed by Fourier-transform infrared (FTIR) spectroscopy. After the air calcination of Co-Co PBA to produce Co_3O_4, the organic ligands in the synthetic process of metal-organic framework are completely removed, as evidenced by the absence of C-H bonds on Co_3O_4 before modification (Figure 2d). In contrast, after functionalizing Co_3O_4 with oleylamine, strong C-H stretching bonds appear at 2916 cm^{-1} and 2845 cm^{-1}. In addition, XRD analysis shows no obvious change in phase composition after modifications and still matches well with the standard Co_3O_4 patterns (Figure S7, Supporting Information). The modification strategy, involving the grafting of long chain oleylamine molecules, effectively transforms the Co_3O_4 surface from hydrophilic to hydrophobic, as evidenced by the phase conversion of the Co_3O_4 dispersion and contact angle measurement. As shown in Figure 2d, distinct from the unmodified Co_3O_4 which tend to disperse in aqueous phase, the ligand grafted Co_3O_4 are inclined to be well dispersed in organic solvent chloroform ($CHCl_3$) stably. In addition, it can be seen from Figure S8a (Supporting Information) that Co_3O_4 shows obvious hydrophilic property before modification. By contrast, when a droplet of water was dripped on the top surface of the Co_3O_4 after modification, the water droplet maintains a ball shape, indicating hydrophobicity property (Figure S8b, Supporting Information). The modified hydrophobic surface benefits the surface wetting compatibility between oleic acid stabilized CdS nanoparticles and Co_3O_4 scaffold. More importantly, the oleylamine molecules tend to bind to the surface of CdS, presumably through hydrogen bonding between functional groups to drive the co-assembly process during the solvent destabilization assembly.

After surface functionalization of Co_3O_4, the ligand-mediated destabilization assembly method was utilized to spontaneously assemble CdS colloidal into the Co_3O_4 framework. The XRD pattern of the CdS/Co_3O_4 assembly in Figure 2e exhibits all the peaks of Co_3O_4 (PDF Card No. 43–1003), while the other three peaks at 26.4°, 43.8° and 52.5° correspond to (111), (220) and (311) facets of face-centered cubic CdS (PDF Card No. 10–0454).[38] X-ray photoelectron spectroscopy (XPS) measurements also clearly illustrate the high-resolution spectra of Cd 3d, S 2p, Co 2p and O 1s of CdS/Co_3O_4 assembly (Figure S9, Supporting Information),[39] indicating the successful dispersion of CdS into the Co_3O_4 nanoboxes. When the CdS/Co_3O_4 assembly was imaged by field emission scanning electron microscopy (FESEM), no obvious changes were observed compared to pure Co_3O_4 (Figure S10a, b, Supporting Information). This can be attributed to the small particle size of CdS, which can hardly be resolved under SEM. Correspondingly, the modification strategy of Co_3O_4 surface with interspersed CdS nanoparticles has an insignificant influence on the morphology and surface roughness of the Co_3O_4 framework. However, the EDX mapping images of the CdS/Co_3O_4 assemblies in Figure S10c, d (Supporting Information) demonstrate the uniform distribution of Cd and S elements apart from Co and O, indicating the effectual dispersion of CdS particles into the Co_3O_4 entire framework.

To further confirm the ordered co-assembly of CdS nanoparticles and Co_3O_4 framework, the CdS/Co_3O_4 assemblies were investigated by high-resolution transmission electron microscopy (HRTEM) and energy dispersive X-ray spectroscopy (EDX) mapping. From Figure S11 (Supporting Information), the porous

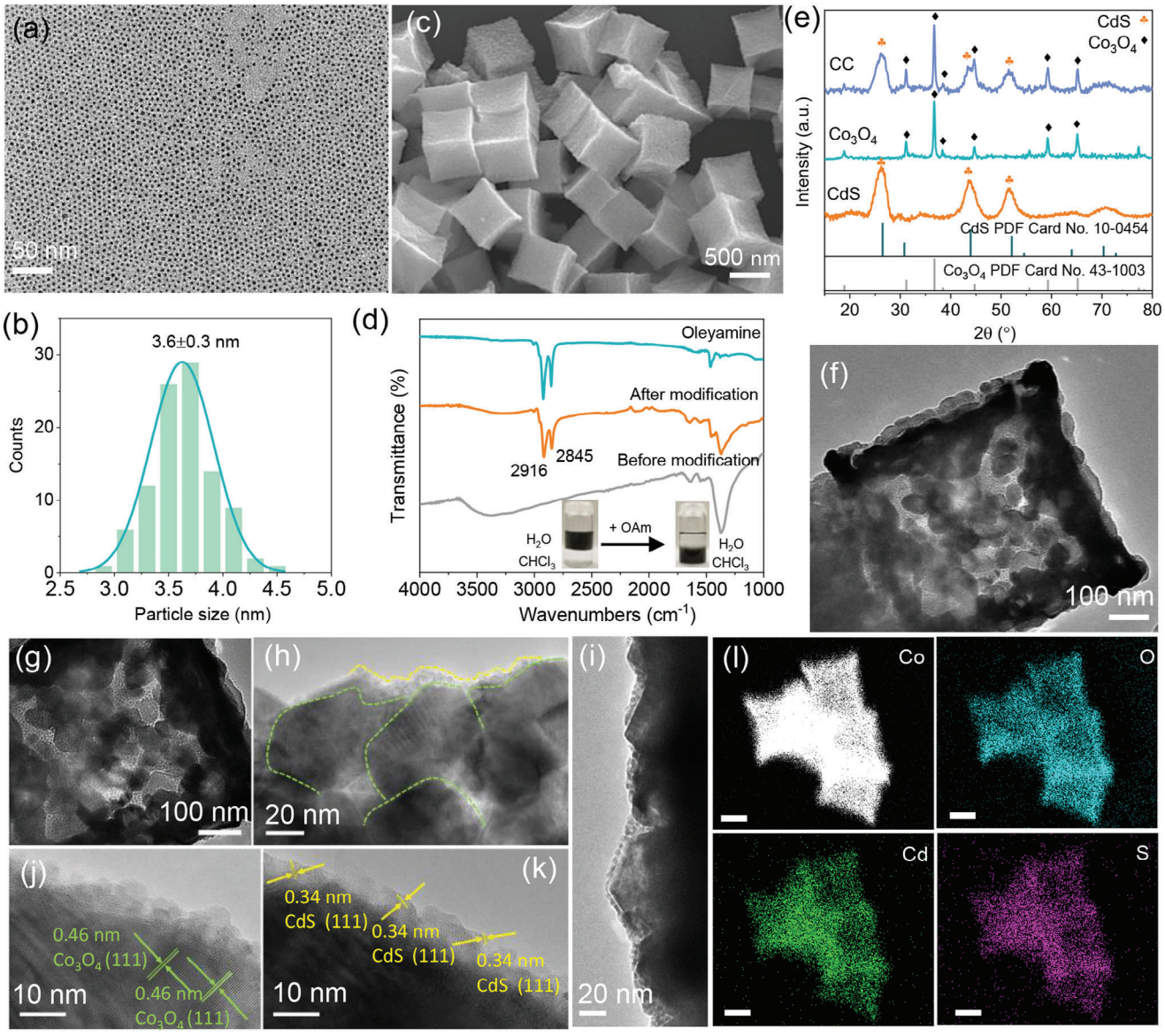

Figure 2. a) TEM image of CdS nanoparticles, b) Particle size distribution profiles of CdS nanoparticles, c) SEM image of 3D Co_3O_4 framework, d) Fourier transform infrared spectra of oleylamine, Co_3O_4 framework before and after modification with oleylamine, the insert in d) is the phase conversion of Co_3O_4 framework before and after modification, e) XRD patterns of CdS, Co_3O_4 and CdS/Co_3O_4 assembly (labelled as CC), f–i) TEM images of CdS/Co_3O_4 assembly at different magnifications, HRTEM images of j) Co_3O_4 part and k) CdS part, l) EDX elemental mapping images of Co, O, Cd, and S (scale bar: 200 nm).

Co_3O_4 structure is observed to be densely packed with small particles. At a higher magnification, it can be clearly observed that the porous interior of Co_3O_4 is occupied and infiltrated with abundant CdS nanoparticles (Figure 2f,g). The alkyl chain group on Co_3O_4, derived from the grafted oleylamine molecules, ideally matches with the oleic acid ligands on the CdS surface, facilitating the efficient and controllable anchorage of CdS nanoparticles onto the Co_3O_4 scaffold. As shown in Figure 2h, compared to the relatively large Co_3O_4 nanoparticles (Figure S3c, d, Supporting Information), small CdS nanoparticles are observed to be uniformly and densely packed within the interior pores of Co_3O_4. Additionally, the CdS nanoparticles are also distributed along the edges of Co_3O_4 framework, resulting from the molecular-recognition effect between the guest CdS and the host Co_3O_4 (Figure 2i). The lattice spacing of 0.46 nm corresponds to (111) plane of Co_3O_4,[40] while 0.34 nm interplanar distances correspond to (111) crystal facet of CdS (Figure 2j,k).[38] Furthermore, the EDX elemental mapping images show the uniform distribution of Cd, S, O, and Co elements, indicating the packed CdS are uniformly distributed throughout the entire Co_3O_4 nanobox, consistent with the SEM results (Figure 2l; Figure S12, Supporting Information). These HRTEM and EDX results substantiate the presence of copious intimately coupled CdS/Co_3O_4 heterojunctions, which are beneficial in inhibiting the recombination of photogenerated carriers.

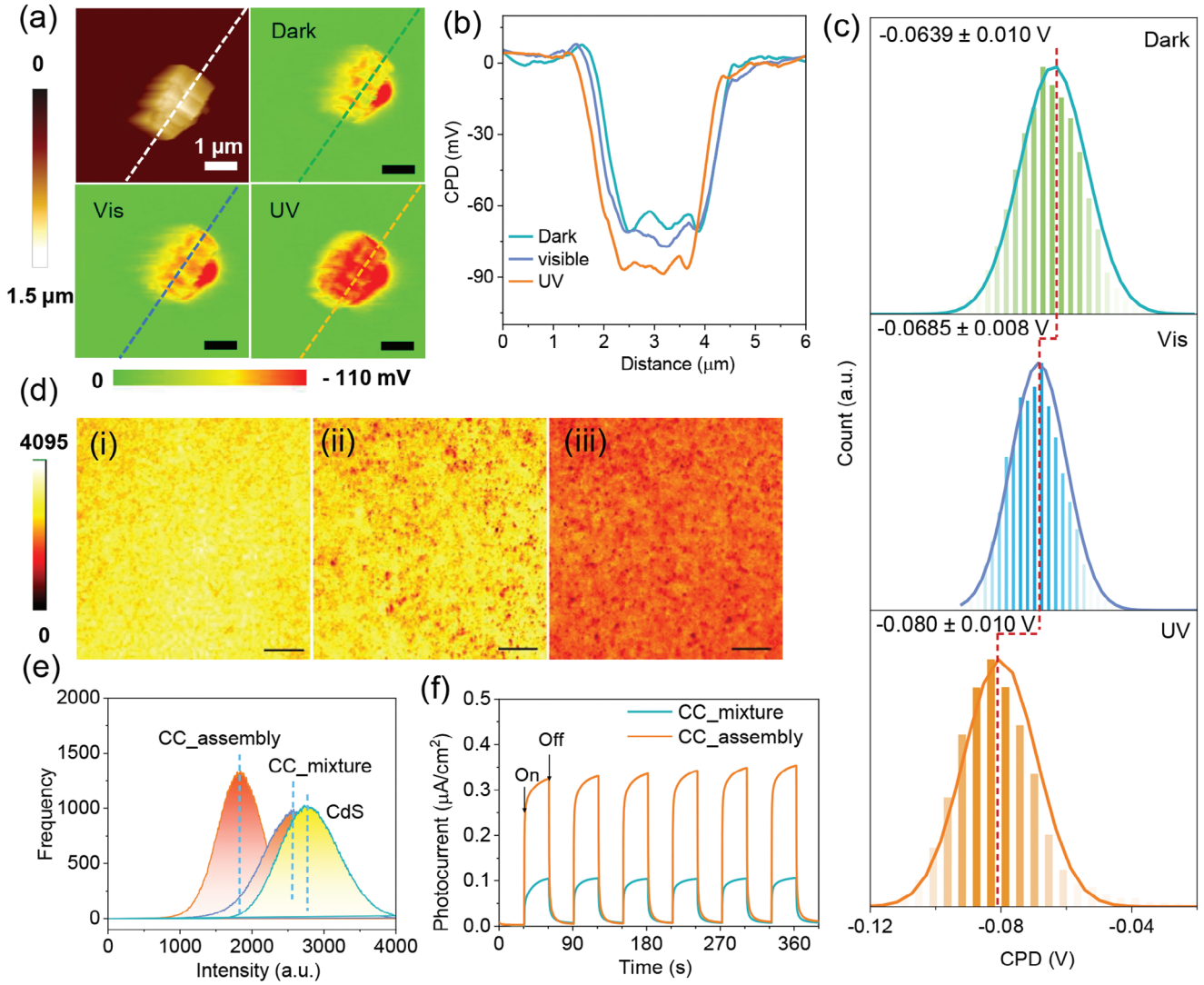

Figure 3. a) Kelvin probe force microscopy (KPFM) topography mapping and contact potential difference (CPD) profiles of CdS/Co_3O_4 assembly in darkness, under visible light, and under UV light irradiation (scale bar: 1 μm), b) Line profiles of CPD along lines marked in (a) in darkness, under visible light and under UV light irradiation, c) Histogram of CPD signals of CdS/Co_3O_4 assembly in darkness, under visible light, and under UV light irradiation, d) confocal fluorescence micrograph of (i) CdS, (ii) CdS/Co_3O_4 mixture, (iii) CdS/Co_3O_4 assembly thin films (488 nm excitation/500–550 nm detection) (scale bar: 50 μm), e) Histogram of confocal fluorescence of CdS, CdS/Co_3O_4 mixture (labelled as CC_mixture) and CdS/Co_3O_4 assembly (labelled as CC_assembly) thin films, f) transient photocurrent response comparison between CdS/Co_3O_4 mixture and CdS/Co_3O_4 assembly.

The self-assembly technique to design and construct heterojunctions will ensure the control of structural arrangement, sufficient interfacial contact between CdS colloids and Co_3O_4 nanoparticles, forming high density particle-to-particle heterojunctions to promote the charge carrier dynamics. To confirm the formation of high density of multi-sites heterojunctions, Kelvin probe force microscopy (KPFM), confocal fluorescence spectroscopy, transient photocurrent response and femtosecond transient absorption spectroscopy (fs-TAS) measurements are carried out to study the recombination dynamics of electron-hole pairs. KPFM will quantitatively measure the contact potential difference (CPD) between the sample surface and tip, providing information about the Fermi level and charge transfer under irradiation.[41,42] When the recombination of photo-induced electron-hole pairs is efficiently inhibited, it will produce a larger contact surface difference under illumination.[43] **Figure 3**a and Figure S13 (Supporting Information) show the topographic mapping and surface potential of the CdS/Co_3O_4 assembly and CdS/Co_3O_4 mixture samples under different light source, respectively. Presumably due to the surface wetting incompatibility between hydrophobic CdS and hydrophilic Co_3O_4, there are no obvious differences in the CPD intensity of CdS/Co_3O_4 mixture in dark, or under visible or UV light conditions (Figure S13, Supporting Information). In contrast, it can be clearly observed from Figure 3a,b that CdS/Co_3O_4 assembly has a low surface potential difference of 63.9 mV in the dark, which slightly increases to 68.5 mV under visible light. When the sample is scanned under UV light, the CPD signal increases

significantly to 80 mV (Figure 3c), which provide evidence of the suppression of electron-hole pairs recombination of the ligand mediated CdS/Co_3O_4 assembly. While KPFM is mainly focused on the electronic characteristics of individual or a few CdS/Co_3O_4 assembly particles, confocal scanning photoluminescence offers a broader perspective on the behavior of photogenerated electron-hole pairs. Hence, CdS, CdS/Co_3O_4 mixture and CdS/Co_3O_4 assembly were prepared as thin films and studied using confocal photoluminescence microscopy.[44] Given that all the samples were prepared using the same spin coating parameters, the film thickness remains unchanged across the different samples (Figure S14, Supporting Information). The intensity of the excitation wavelength is kept constant, allowing the observed variations in photoluminescence (PL) intensity to be attributed to differences in the recombination kinetics of charge carriers. From Figure 3d,e, it can be observed that the CdS film exhibits a significantly higher PL intensity, along with a uniform distribution in emission. This observation suggests a pronounced recombination of electrons and holes of CdS. The introduction of Co_3O_4 and its direct mixing with CdS, slightly decreases the PL intensity for the CdS/Co_3O_4 mixture. Conversely, the CdS/Co_3O_4 assembly shows a substantially lowered PL intensity compared to CdS and CdS/Co_3O_4 mixture, demonstrating the considerably suppressed charge recombination. This phenomenon is further supported by the transient photocurrent response results (Figure 3f), where the photocurrent intensity of the CdS/Co_3O_4 assembly is almost three times greater than that of the CdS/Co_3O_4 mixture. This indicates enhanced charge transfer kinetics via the self-assembled heterostructures formation of CdS and Co_3O_4. The CdS nanoparticles are dispersed both on the exterior and within the interior pores of Co_3O_4 framework, forming high density particulate heterojunctions and intimate interfacial contact between the CdS guest and Co_3O_4 host.

It is crucial to understand the correlations between charge carrier transfer and multi-sites heterojunctions to achieve enhanced photoactivity. The ultrafast carrier dynamics are further evaluated using femtosecond transient absorption spectroscopy (fs-TAS). The decay of substances from excited state to ground state will be analyzed and thus the transitions between different energy levels such as energy transfer and electron transfer phenomenon can be investigated. The transient absorption spectra of excited states over time, including excited-state absorption (ESA), ground-state bleach (GSB) and stimulated emission (SE) are obtained.[45,46] Specifically, the ESA signal is ascribed to light absorption of electrons in an excited state.[47] The introduction of Co_3O_4 will serve as the hole scavenger, effectively capturing the generated holes to promote an increase in the number of excited electrons. As a result, the positive ESA signals of CdS/Co_3O_4 mixture and CdS/Co_3O_4 assembly are of higher intensity compared to pure CdS (**Figure** 4a–c). Similarly, the GSB signal reflects the number of photoinduced electrons and a stronger GSB signal indicates the generation of more charge carriers. Interestingly, CdS has a weaker negative GSB signal of −0.024 (Figure 4d), while the GSB signals of the CdS/Co_3O_4 mixture and CdS/Co_3O_4 assembly can reach as low as −0.035 and −0.043, respectively (Figure 4e,f). The stronger GSB signal observed in the CdS/Co_3O_4 heterojunction indicates that the introduction of Co_3O_4 porous scaffold not only serves as a versatile host to encapsulate CdS active species, but also interacts with CdS to facilitate efficient the charge carrier transfer. It is worth noting that the assemble of CdS colloidal particles into Co_3O_4 scaffold forms high-density particulate heterojunctions via the proposed self-assembly method. As a result, more charge carriers can be photogenerated for CdS/Co_3O_4 assembly compared to the CdS/Co_3O_4 mixture. The SE signals remain nearly unchanged, indicating the limited hole transfer efficiency of CdS. The kinetic fitting of the GSB decay time at 450 nm for CdS, CdS/Co_3O_4 mixture and CdS/Co_3O_4 assembly are shown in Figure 4g and the fitting parameters are recorded in Table S1 (Supporting Information). The shorter decay time ≈1306.8 ps of CdS origins from the fast recombination of free photoinduced electron-hole pairs. Conversely, the slower decay indicates a reduced recombination rate, allowing the electrons to readily participate in redox reactions rather than recombining with holes. Therefore, the average decay times of CdS/Co_3O_4 mixture and CdS/Co_3O_4 assembly are prolonged to 1508.7 ps and 1564.9 ps, respectively, indicating that Co_3O_4 can effectively prohibit the charge carrier recombination and the formed multi-sites heterojunctions will further promote the charge carrier kinetics.

This ligand mediated assembly approach can be extended as a general approach for constructing heterojunctions between CdS colloids with other MOF derived hosts, without being limited to the regularity of the Co_3O_4 framework or the composition of MOF derived scaffold. To demonstrate its universality, we applied the assembly method to include PBA-derived Co_3O_4 framework and other MOF derived scaffolds with less regular constitutions. When the Co-Co PBA was calcined at a higher temperature of 700 °C, resulting in deformed Co_3O_4, the CdS colloids will still densely and uniformly distributed along the irregular cubic shape of the deformed Co_3O_4 framework (Figure S15, Supporting Information). In addition, when the MOF substrate is replaced with ZIF-67 to produce Co_3O_4 support, the assembly of CdS nanoparticles still successfully forms the particle-to-particle heterojunctions with minimal changes (Figure 4h; Figure S16, Supporting Information). To further explore the versatility of the assembly method, ZIF-8 derived ZnO, cubic ZIF-8 derived cubic ZnO and MIL-125 derived TiO_2 were also synthesized and employed as supports for the assembly with CdS (Figures S17, S18, S19, Supporting Information). Likewise, CdS is dispersed in both the interior and exterior pores of different MOF derived frameworks, forming outlying and immediate interfacial contact leading to multi-sites heterojunctions between the guest and host (Figure 4h; Figure S20, Supporting Information). These results demonstrate that the ligand mediated assembly method is not restricted to the shape or the composition of scaffolds, indicating its suitability for assembling nanoparticles into 3D porous and tortuous structures, thus forming high-density heterojunctions.

As a typical case study, the photocatalytic CO_2 reduction performance of pure CdS, PBA derived Co_3O_4, and CdS/PBA derived Co_3O_4 assembly with various composition ratios were studied under the same conditions. It can be seen from **Figure** 5a that bare CdS and Co_3O_4 show relatively low CO production rates of merely 2.7 μmol g^{-1} h^{-1} and 15 μmol g^{-1} h^{-1}, respectively. By contrast, all CdS/Co_3O_4 assemblies show improved photocatalytic activity, by virtue of the constructed heterojunction between CdS and Co_3O_4. The optimal sample with 40% loading of Co_3O_4 exhibits the highest CO production rate of 73.9 μmol g^{-1} h^{-1} and CO selectivity of 98.9%. However, an insufficient loading of Co_3O_4 will lead to an excessive accumulation

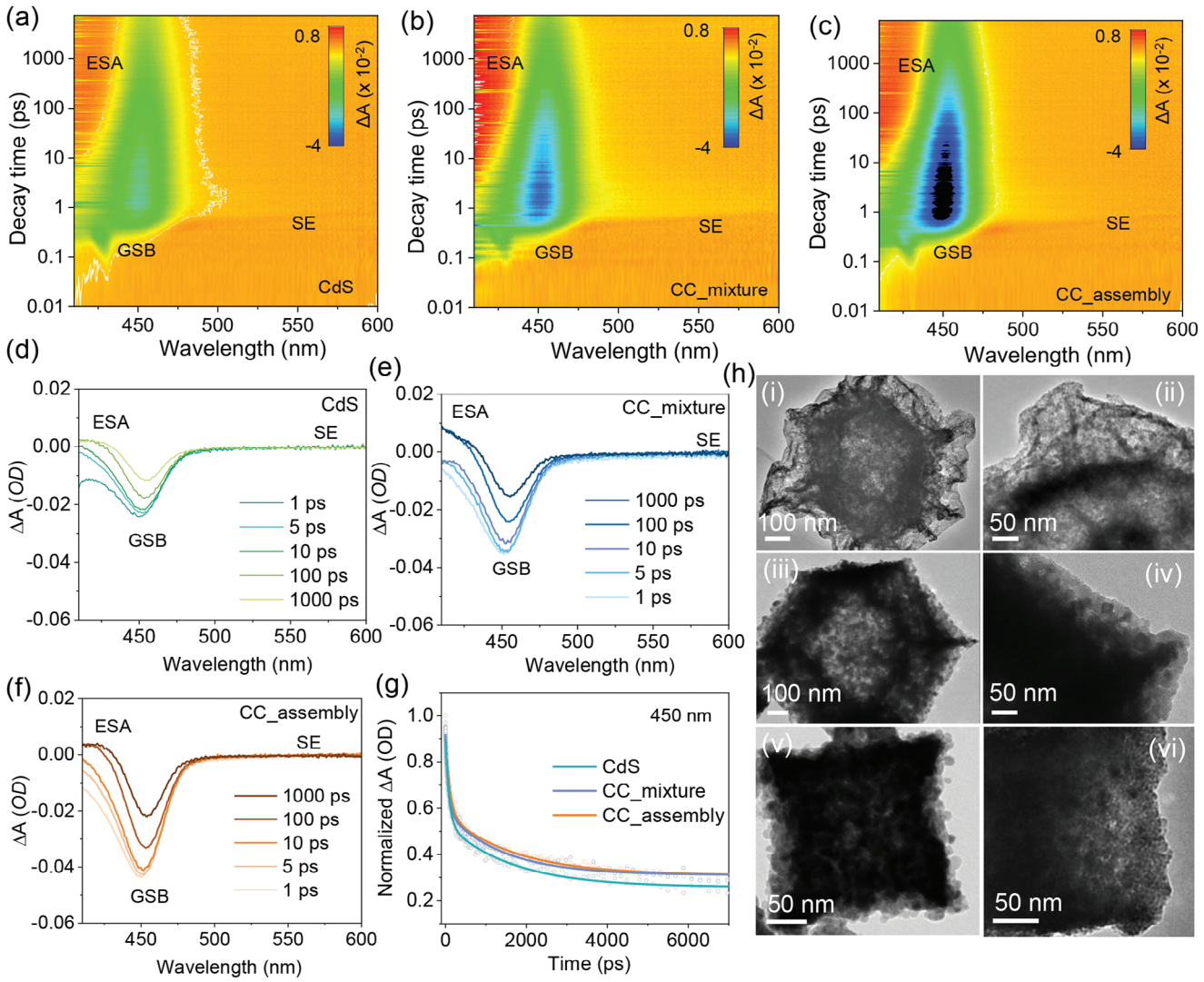

Figure 4. 2D transient absorption surface plots of a) CdS colloids, b) CdS/Co_3O_4 mixture (labelled as CC_mixture), c) CdS/Co_3O_4 assembly (labelled as CC_assembly). Transient absorption signals of d) CdS colloids, e) CdS/Co_3O_4 mixture, f) CdS/Co_3O_4 assembly. g) The decay signals of CdS, CdS/Co_3O_4 mixture and CdS/Co_3O_4 assembly monitored at 450 nm. h) CdS colloids assembling with other MOF derived hosts: (i, ii) TEM images at different magnifications of CdS/ZIF 67 derived Co_3O_4 assembly, (iii, iv) TEM images at different magnifications of CdS/ZIF 8 derived ZnO assembly, (v, vi) TEM images at different magnifications of CdS/cubic ZIF 8 derived cubic ZnO assembly.

of CdS on the Co_3O_4 surface (Figure S21, Supporting Information), affecting the light absorption and shortening active photoelectron lifetime for proton reduction. Conversely, overloading of Co_3O_4 would leads to insufficient charge transfer and active sites (Figure S22, Supporting Information). This stark contrast highlights the importance of designing and constructing intimate heterointerface contact that is commensurate with the host-guest proportion. Moreover, the significant difference in CO production activity between the CdS/Co_3O_4 mixture and CdS/Co_3O_4 assembly further validates the effectiveness of constructing multi-sites heterojunctions via self-assembly approach (Figure S23, Supporting Information). These results are consistent with the previous findings on charge transfer dynamics shown in Figure 4. To further confirm the carbon and oxygen sources of the photocatalytic activity, ^{13}C and ^{18}O isotope labelling experiments were carried out.[48,49] Labelled $^{13}CO_2$ produced from $Na_2{}^{13}CO_3$ and $^{12}CO_2$ as the control gas were used to trace the carbon source and ^{18}O isotope from $H_2{}^{18}O$ was used to track the oxygen source. All the products from the photocatalytic process were injected into gas chromatography-mass spectrometry (GC-MS) for analysis. It is apparent from Figure 5b that m/z of CO from ^{13}C labelled $^{13}CO_2$ gas is 29, while the m/z of CO coming from $^{12}CO_2$ is 28, indicating that the carbon of CO comes from CO_2 gas, therefore validating the reliability of the above photoreduction performance.[50] On the other hand, the existence of $^{16}O^{18}O$ and $^{18}O_2$ has confirmed that water oxidation occurred as the other half reaction to consume the photo-generated holes (Figure 5b). In addition, liquid ^1H NMR results indicate that there is no obvious peak associated with liquid product (Figure S24, Supporting Information). The photocatalytic CO_2 reduction performances at different light wavelengths were studied (Figure 5c). It displays a high CO production rate

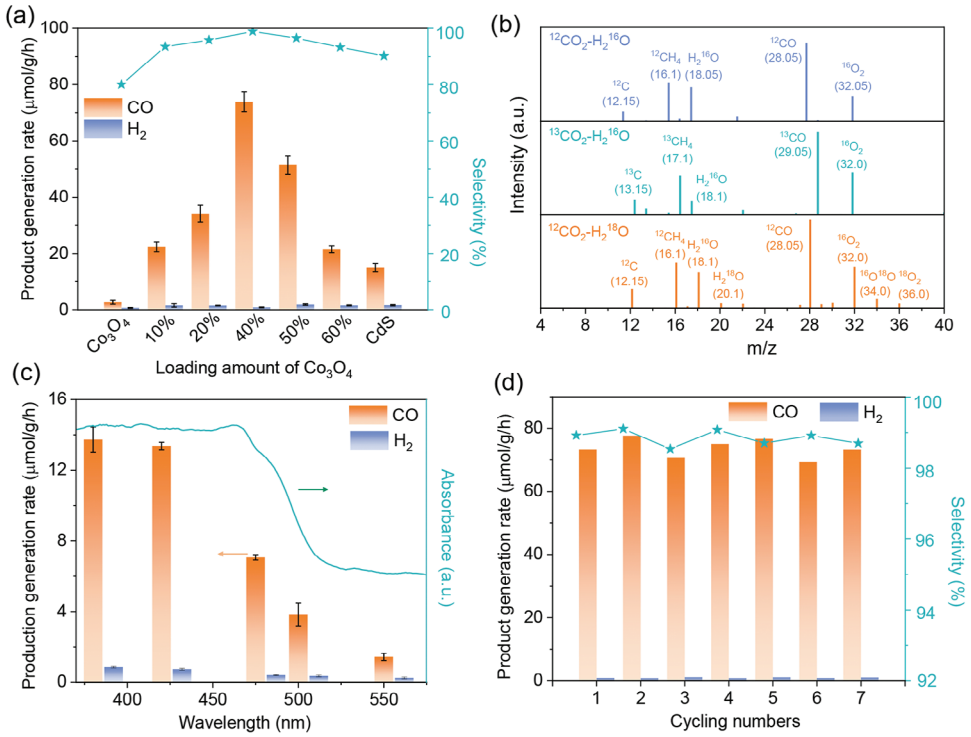

Figure 5. a) Photocatalytic CO_2 reduction performance of CdS/Co_3O_4 assemblies with different loading amounts of Co_3O_4. b) ^{13}C and ^{18}O isotopic experiments of CdS/40% Co_3O_4 assembly sample based on GC-MS results. c) Photocatalytic CO_2 reduction performance of CdS/40% Co_3O_4 sample under different wavelengths. d) Stability test of the CdS/40% Co_3O_4 assembly sample.

under UV light (380 nm), and decreases by half under visible light of 420 nm and 475 nm. Once the light wavelength exceeds the light absorption edge of CdS at 500 nm, the CO production rate becomes negligible, which is consistent with the subsequent light absorption analysis. The self-assembly CdS/Co_3O_4 composite catalyst also displays a very stable CO_2 reduction activity, maintaining a CO production rate at around 73.3 μmol g^{-1} h^{-1} even after seven cycles (Figure 5d). This highly efficient and stable catalyst demonstrates the superiority and consistency of the proposed strategy to construct a high density of heterojunctions between packed CdS nanoparticles and the modified porous Co_3O_4 framework.

After obtaining the well-confined CdS/Co_3O_4 assembly and observing a significantly improved catalytic activity, a series of characterizations were performed to understand the mechanisms and correlations that contributed to the enhanced performance. Considering the three main steps of photocatalytic process involving photon absorption to produce photo-generated electron-hole pairs, separation of electrons and holes, and surface redox reactions, the light absorption capability was first investigated using UV–vis absorption spectroscopy. As shown in **Figure 6a**, CdS shows a limited visible light absorption with a maximum absorption edge extended to 519 nm. Contrarily, Co_3O_4, a black color material, exhibits superior light absorption from UV to visible light. As a result, when CdS was encapsulated within the interior and exterior pores of Co_3O_4 scaffold, its light absorption in the visible light range significantly improved due to the presence of Co_3O_4. This improved broadband light absorption is highly beneficial for photocatalytic CO_2 reduction.

Subsequently, the charge transfer kinetics and mechanism were investigated using photo/electrochemical techniques. From the photocurrent results in Figure 6b, it can be seen the photocurrents of all samples respond rapidly when the light is switched on and immediately drop to almost zero when the light is turned off. This demonstrates that the generation of charge carriers is strongly dependent on the presence of light. Notably, CdS/Co_3O_4 exhibits a much higher photocurrent than bare CdS and Co_3O_4, indicating the enhanced charge transfer kinetics of CdS/Co_3O_4 assembly. Simultaneously, the Nyquist plots show that CdS/Co_3O_4 assembly exhibits a smaller arc radius compared to CdS (Figure 6c). This decrease in arc radius signifies a lower resistance in the interfacial charge migration, attributed to the good conductivity of Co_3O_4 (the smallest semicircle). Fluorescence (FL) spectra was then employed to study the recombination phenomenon of electrons and holes. Due to the uniform particle sizes of the as-prepared CdS, pure CdS nanoparticles exhibit a fairly narrow peak at 473 nm (Figure 6d). Comparatively, the FL intensity of the CdS/Co_3O_4 assembly decreased by more than half, revealing its effective inhibition of photo-induced electrons and holes recombination. Based on the obtained photocurrent, Nyquist plots and fluorescence spectra, it is evident that the introduction of Co_3O_4 framework can significantly promote the charge transfer and separation of CdS, favorable for the photocatalytic CO_2 reduction activity.

Given that photocatalytic CO_2 reduction is a gas-liquid-solid interfacial reaction, the adsorption of CO_2 reactant gas is a crucial step for the subsequent catalytic reaction. CO_2 temperature-programmed desorption (TPD) characterization is employed to

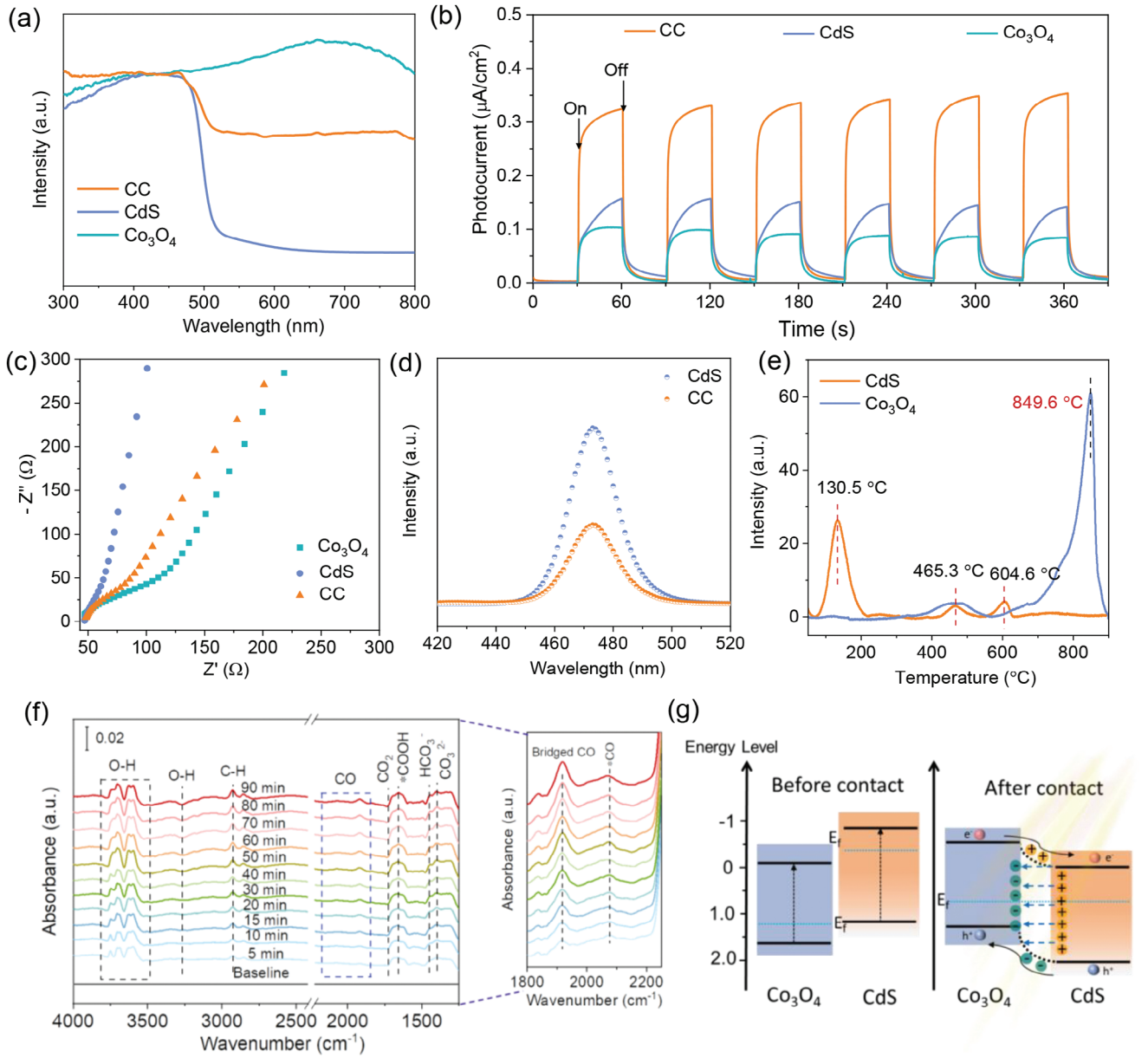

Figure 6. a) UV–vis absorption spectra of CdS, Co_3O_4, and CdS/40% Co_3O_4 assembly (labelled as CC). b) Photocurrent response of CdS, Co_3O_4, and CdS/40% Co_3O_4 assembly for repeated light on-and-off cycles. c) Nyquist plots of CdS, Co_3O_4, and CdS/40% Co_3O_4 assembly. d) Fluorescence spectra of CdS and CdS/40% Co_3O_4 assembly. e) CO_2-TPD profiles of CdS and Co_3O_4, f) Photocatalytic CO_2 reduction DRIFTS experiments over CdS/40% Co_3O_4 assembly in the presence of CO_2 and H_2O under irradiation, g) Proposed charge transfer process of CdS/Co_3O_4 composites.

study the CO_2 adsorption capacity of the catalysts. It can be observed from Figure 6e that CdS desorbs CO_2 gas at a low temperature of 130.5 °C, demonstrating the relatively weak affinity between CO_2 and CdS surface. When the temperature increases to 400–600 °C, the functional groups on the CdS surface will decompose and release gas, resulting in two desorption peaks in the range of 400 to 600 °C. In contrast, Co_3O_4 desorbs CO_2 gas at a high temperature of 849.6 °C, and the signal intensity is much higher than that of CdS, indicating that Co_3O_4 can adsorb a significant amount of CO_2. These results suggest Co_3O_4 has a better CO_2 adsorption ability than CdS, which favors the photocatalytic CO_2 reduction process.

The introduction of Co_3O_4 not only serves as a porous framework to homogeneously and spontaneously assemble CdS nanoparticles, it also facilitates several crucial steps in photocatalytic CO_2 reduction. These include light absorption, separation of photo-induced electrons and holes, and surface reaction kinetics to promote CO_2 adsorption. These factors underscore the significant contribution of Co_3O_4 to the overall photocatalytic CO_2 reduction process. To further investigate the CO_2 photoreduction, diffuse reflectance infrared Fourier transform spectroscopy (DRIFTS) was used to track the pivotal intermediates during the adsorption, activation and reaction of CO_2 on the surface of the CdS/Co_3O_4 assembly under light illumination (Figure 6f).

The observed formation of chemically absorbed CO_2 (1260 cm^{-1}, 1700 cm^{-1}), bicarbonates (HCO_3^-, 1430–1440 cm^{-1}) and carbonate (CO_3^{2-}, 1300–1324 cm^{-1}) can be attributed to the absorption interaction between CO_2 molecules and the photocatalysts.[51] The observation of augmented peaks at 1800–1875 cm^{-1} and 2142 cm^{-1} are assigned to the weak multi-bonded CO and the final product of CO, indicating the accumulative production of CO during the CO_2 photoreduction. Importantly, the infrared peak at 1624 cm^{-1} corresponds to the formation of COOH*, which is a critical intermediate in the CO_2 reduction to CO.[52] This result agrees with the high CO selectivity of 98.9%, suggesting that COOH* intermediates play a significant role in the CO_2 conversion to CO.

To further study the corresponding heterojunction structure and propose a possible charge transfer mechanism, Mott-Schottky (M-S) characterization was used to reveal the type and band structure of each individual semiconductor. The M-S curve displays a negative slope of CdS, indicating its n-type characteristics, while Co_3O_4 exhibits a distinctly positive slope, suggesting it is a p-type semiconductor (Figure S25, Supporting Information). From the flat potentials obtained from the M-S curves, the conduction band (CB) potential of n-type CdS and valence band (VB) potential of p-type Co_3O_4 are determined to be −1.05 eV and 1.40 eV, respectively. Taken together with their bandgap calculation based on the UV–vis absorption results (Figure S26, Supporting Information), the VB level of CdS and the CB level of Co_3O_4 can be deduced and the respective band structures are shown in Figure 6g. Upon light excitation, both CdS and Co_3O_4 will generate electrons at the CB and leave behind holes at the VB. The coupling of the n-type CdS and p-type Co_3O_4 forms a p-n junction, inducing an internal electric field that drives the transfer of electrons from Co_3O_4 to CdS and holes from CdS to Co_3O_4. These separated electrons are then involved in the photocatalytic CO_2 reduction to reduce CO_2 to CO, while the holes are consumed by H_2O.[53] To further confirm the charge transfer mechanism, density function theory calculation was applied to obtain the Fermi levels and work functions of CdS and Co_3O_4 (Figure S27, Supporting Information). As shown in Figure S27a and b (Supporting Information), the work function of CdS and Co_3O_4 were calculated as 4.70 eV and 5.14 eV, respectively. Before contact, the Fermi level of CdS is above that of Co_3O_4, which is consistent with their n-type and p-type semiconductor property. Upon contact, the free electrons will transfer from CdS to Co_3O_4 until the Fermi levels are aligned and form an internal electric field from CdS to Co_3O_4 at their interface (Figure S27c, Supporting Information). The electric field will drive the transfer of electrons from Co_3O_4 to CdS and holes from CdS to Co_3O_4.

3. Conclusion

In conclusion, we have developed a ligand grafted method to spontaneously assemble 0D CdS nanoparticles within 3D MOF derived porous framework to materialize heterostructure ensemble for efficient photocatalytic CO_2 reduction. The grafted ligand modifies the hydrophilicity of the Co_3O_4 surface, enabling molecular recognition of CdS nanoparticles to effectuate homogeneous assembly of CdS on the interior and exterior surface of Co_3O_4 framework. The engineered ordered microstructure creates high-density heterojunctions and promotes the separation and transport of photo-induced charge carriers, thereby achieving an efficient photocatalytic CO_2 reduction activity. In addition, the proposed ligand grafting method can be generalized to achieve spontaneous assembly of CdS colloids with various metal organic framework derived porous scaffolds. The ordered co-assembly and the exceptional photocatalytic CO production performance of CdS/Co_3O_4 assembly underscores the potential of this direct and simple assembly strategy in exploring a new avenue to tailor heterointerfaces for diverse energy conversion applications.

Supporting Information

Supporting Information is available from the Wiley Online Library or from the author.

Acknowledgements

T.Z. and T.L. contributed to this work equally. The authors gratefully thank the financial support from the A*STAR, RIE2025 Manufacturing, Trade and Connectivity (MTC), M22K2c0081 and A*STAR Low Carbon Energy Research (LCER) Funding Initiative (FI) project (Award ID: U2102d2011, A-8000278-00-00).

Conflict Of Interest

The authors declare no conflict of interest.

Data Availability Statement

The data that support the findings of this study are available in the supplementary material of this article.

Keywords

cadmium sulfide, charge transfer, CO_2 reduction, heterojunction, self-assembly

Received: January 24, 2024
Published online:

[1] Q. Wang, S. Kalathil, C. Pornrungroj, C. D. Sahm, E. Reisner, *Nat. Catal.* **2022**, *5*, 633.
[2] S. Cestellos-Blanco, H. Zhang, J. M. Kim, Y.-x. Shen, P. Yang, *Nat. Catal.* **2020**, *3*, 245.
[3] D. Li, M. Kassymova, X. Cai, S.-Q. Zang, H.-L. Jiang, *Coord. Chem. Rev.* **2020**, *412*, 213262.
[4] X. Wu, N. Luo, S. Xie, H. Zhang, Q. Zhang, F. Wang, Y. Wang, *Chem. Soc. Rev.* **2020**, *49*, 6198.
[5] S. W. L. Ng, M. Gao, W. Lu, M. Hong, G. W. Ho, *Adv. Funct. Mater.* **2021**, *31*, 2104750.
[6] C. Wu, N. Corrigan, C. H. Lim, W. Liu, G. Miyake, C. Boyer, *Chem. Rev.* **2022**, *122*, 5476.
[7] A. Wagner, C. D. Sahm, E. Reisner, *Nat. Catal.* **2020**, *3*, 775.
[8] M. Gao, T. Zhang, G. W. Ho, *Nano Res.* **2022**, *15*, 9985.
[9] T. Zhang, F. Meng, M. Gao, W. L. Ong, K. G. Haw, T. Ding, G. W. Ho, S. Kawi, *EcoMat* **2021**, *3*, e12152.

[10] L. Wang, B. Zhu, J. Zhang, J. B. Ghasemi, M. Mousavi, J. Yu, *Matter* **2022**, *5*, 25.
[11] T. Zhang, F. Meng, M. Gao, J. Wei, K. J. H. Lim, K. H. Lim, P. Chirawatkul, A. S. W. Wong, S. Kawi, G. W. Ho, *Small* **2023**, *19*, 2301121.
[12] C. M. Fung, B. J. Ng, C. C. Er, W. K. Chong, J. Low, X. Guo, X. Y. Kong, H. W. Lee, L. L. Tan, A. R. Mohamed, S. P. Chai, *Small Struct.* **2023**, *4*, 2300083.
[13] Z. Wang, Z. Lin, S. Shen, W. Zhong, S. Cao, *Chin. J. Catal.* **2021**, *42*, 710.
[14] G. Zhang, Z. Wang, J. Wu, *Nanoscale* **2021**, *13*, 4359.
[15] G. W. Ho, A. T. S. Wee, J. Lin, *Appl. Phys. Lett.* **2001**, *79*, 260.
[16] Z. Li, Q. Fan, Z. Ye, C. Wu, Z. Wang, Y. Yin, *Science* **2023**, *380*, 7.
[17] L. Ran, Z. Li, B. Ran, J. Cao, Y. Zhao, T. Shao, Y. Song, M. K. H. Leung, L. Sun, J. Hou, *J. Am. Chem. Soc.* **2022**, *144*, 17097.
[18] Z. Jiang, X. Xu, Y. Ma, H. S. Cho, D. Ding, C. Wang, J. Wu, P. Oleynikov, M. Jia, J. Cheng, Y. Zhou, O. Terasaki, T. Peng, L. Zan, H. Deng, *Nature* **2020**, *586*, 549.
[19] Y. Wang, G. Fan, S. Wang, Y. Li, Y. Guo, D. Luan, X. Gu, X. W. D. Lou, *Adv. Mater.* **2022**, *34*, 2204865.
[20] J. Tian, Y. Zhang, L. Du, Y. He, X. H. Jin, S. Pearce, J. C. Eloi, R. L. Harniman, D. Alibhai, R. Ye, D. L. Phillips, I. Manners, *Nat. Chem.* **2020**, *12*, 1150.
[21] J. Fonseca, L. Meng, I. Imaz, D. Maspoch, *Chem. Soc. Rev.* **2023**, *52*, 2528.
[22] F. Zhang, R. Liu, Y. Wei, J. Wei, Z. Yang, *J. Am. Chem. Soc.* **2021**, *143*, 11662.
[23] T. Li, B. Xue, B. Wang, G. Guo, D. Han, Y. Yan, A. Dong, *J. Am. Chem. Soc.* **2017**, *139*, 12133.
[24] S. Rodriguez-Jimenez, H. Song, E. Lam, D. Wright, A. Pannwitz, S. A. Bonke, J. J. Baumberg, S. Bonnet, L. Hammarstrom, E. Reisner, *J. Am. Chem. Soc.* **2022**, *144*, 9399.
[25] Z. Li, Q. Fan, Y. Yin, *Chem. Rev.* **2022**, *122*, 4976.
[26] M. Dijkstra, E. Luijten, *Nat. Mater.* **2021**, *20*, 762.
[27] B. Wang, J. Yu, L. Sui, S. Zhu, Z. Tang, B. Yang, S. Lu, *Adv. Sci.* **2020**, *8*, 2001453.
[28] N. Li, L. Han, H. Zhang, J. Huang, X. Luo, X. Li, Y. Wang, W. Qian, Y. Yang, *Nano Res.* **2022**, *15*, 8836.
[29] A. B. Grommet, M. Feller, R. Klajn, *Nat. Nanotechnol.* **2020**, *15*, 256.
[30] L. Cheng, Q. Xiang, Y. Liao, H. Zhang, *Energy Environ. Sci.* **2018**, *11*, 1362.
[31] L. Wang, J. Wan, Y. Zhao, N. Yang, D. Wang, *J. Am. Chem. Soc.* **2019**, *141*, 2238.
[32] Q. Zhang, P. Yang, H. Zhang, J. Zhao, H. Shi, Y. Huang, H. Yang, *Appl. Catal. B* **2022**, *300*, 120729.
[33] M. Li, S. Zhang, L. Li, J. Han, X. Zhu, Q. Ge, H. Wang, *ACS Sustainable Chem. Eng.* **2020**, *8*, 11465.
[34] C. Han, X. Zhang, S. Huang, Y. Hu, Z. Yang, T. T. Li, Q. Li, J. Qian, *Adv. Sci.* **2023**, *10*, 2300797.
[35] R. Zeng, K. Lian, B. Su, L. Lu, J. Lin, D. Tang, S. Lin, X. Wang, *Angew. Chem., Int. Ed.* **2021**, *60*, 25055.
[36] G. Yilmaz, S. B. Peh, D. Zhao, G. W. Ho, *Adv. Sci.* **2019**, *6*, 1901129.
[37] Y. Lu, W. Zhan, Y. He, Y. Wang, X. Kong, Q. Kuang, Z. Xie, L. Zheng, *ACS Appl. Mater. Interfaces* **2014**, *6*, 4186.
[38] G. S. Kenath, P. Maity, Y. Kumar, H. Kumar, V. K. Gangwar, S. Chaterjee, S. Jit, A. K. Ghosh, B. N. Pal, *J. Mater. Chem. C* **2017**, *5*, 9792.
[39] Z. Chen, J. Pan, J. Mei, Q. Yu, P. Wang, P. Wang, J. Wang, C. Song, Y. Zheng, C. Li, *J. Environ. Chem. Eng.* **2021**, *9*, 104895.
[40] H. Zhou, B. Lv, D. Wu, Y. Xu, *CrystEngComm* **2013**, *15*, 8337.
[41] H. S. Moon, K. C. Hsiao, M. C. Wu, Y. Yun, Y. J. Hsu, K. Yong, *Adv. Mater.* **2023**, *35*, 2200172.
[42] H. Wu, H. Si, Z. Zhang, Z. Kang, P. Wu, L. Zhou, S. Zhang, Z. Zhang, Q. Liao, Y. Zhang, *Adv. Sci.* **2018**, *5*, 1801219.
[43] G. Wang, L. Li, W. Fan, R. Wang, S. Zhou, J.-T. Lü, L. Gan, T. Zhai, *Adv. Funct. Mater.* **2018**, *28*, 1800339.
[44] Y. Yang, H. Peng, C. Liu, Z. Arain, Y. Ding, S. Ma, X. Liu, T. Hayat, A. Alsaedi, S. Dai, *J. Mater. Chem. A* **2019**, *7*, 6450.
[45] W. Wang, X. Bai, Q. Ci, L. Du, X. Ren, D. L. Phillips, *Adv. Funct. Mater.* **2021**, *31*, 2103978.
[46] Y. Zhao, P. Zhang, Z. Yang, L. Li, J. Gao, S. Chen, T. Xie, C. Diao, S. Xi, B. Xiao, C. Hu, W. Choi, *Nat. Commun.* **2021**, *12*, 3701.
[47] C. Bie, B. Zhu, L. Wang, H. Yu, C. Jiang, T. Chen, J. Yu, *Angew. Chem., Int. Ed.* **2022**, *61*, 202212045.
[48] S. Wang, B. Jiang, J. Henzie, F. Xu, C. Liu, X. Meng, S. Zou, H. Song, Y. Pan, H. Li, J. Yu, J. Ye, *Nat. Commun.* **2023**, *14*, 2534.
[49] F. Xu, K. Meng, B. Cheng, S. Wang, J. Xu, J. Yu, *Nat. Commun.* **2020**, *11*, 4613.
[50] P. Hu, G. Liang, B. Zhu, W. Macyk, J. Yu, F. Xu, *ACS Catal.* **2023**, *13*, 12623.
[51] H. Li, C. Cheng, Z. Yang, J. Wei, *Nat. Commun.* **2022**, *13*, 6466.
[52] Y. Cao, L. Guo, M. Dan, D. E. Doronkin, C. Han, Z. Rao, Y. Liu, J. Meng, Z. Huang, K. Zheng, P. Chen, F. Dong, Y. Zhou, *Nat. Commun.* **2021**, *12*, 1675.
[53] Q. Xu, L. Zhang, B. Cheng, J. Fan, J. Yu, *Chem* **2020**, *6*, 1543.